Simulation of strong vibro-acoustic coupling effects in ducts using a partitioned approach in the time domain

J. Kersschot [1,2], **H. Denayer** [1,2], **W. De Roeck** [1], **W. Desmet** [1,2]
[1] KU Leuven, Department of Mechanical Engineering,
Celestijnenlaan 300, B-3001, Heverlee, Belgium
e-mail: **jurgen.kersschot@kuleuven.be**

[2] DMMS Lab, Flanders Make
Belgium

Abstract

In the search for better noise abatement solutions in flow ducts, a better understanding of the interaction between unsteady aerodynamics, the acoustic field and the dynamics of the confining structure is required. Due to the large differences in time and length scales, a monolithic simulation of this multiphysical interaction would result in high computational loads. A more efficient option is a partitioned approach, which means coupling domain-dedicated solvers. This paper focuses on the vibro-acoustic coupling in the time domain between a flow-acoustic solver for the linearized Euler equations and a structural solver for the Euler-Bernoulli beam equation. These two solvers, using different spatial and temporal discretization schemes, are coupled through the open-source library preCICE and run in a co-simulation. A 2D verification case is simulated and compared to the results of a commercial monolithic solver in the frequency domain, showing that the partitioned approach properly captures the mutual interaction between duct acoustics and structural vibrations.

1 Introduction

Lightweight materials are entering the industrial practice for flow-confining structures, such as ventilation ducts and automotive exhaust systems. Unfortunately, such lightweight constructions typically exhibit poor vibro-acoustic properties and unsteady pressure fluctuations in the flow can easily excite structural vibrations. These vibrations lead to unwanted noise emissions, which are often only discovered after installation. This limits the possibilities for noise mitigation to adding heavy damping layers, compromising the lightweight design.

The pressure fluctuations causing the vibrations can have an aerodynamic or acoustic nature. Several semi-analytic models describe how a turbulent flow excites a flexible structure through aerodynamic wall pressure fluctuations [1]. For the vibro-acoustic interaction between propagating acoustic waves and a flexible confining structure, analytical models for simple duct geometries exist [2, 3, 4, 5]. To describe the interaction between flow, acoustics and structural vibrations both the vibro-acoustic and aero-elastic interaction should be considered. David *et al.* [6] therefore proposed a semi-analytical model, summing the aero-elastic and vibro-acoustic contributions. However, such a semi-analytical model is limited to simple duct geometries.

Numerical models allow studying the multiphysical interactions for any kind of duct geometries. For the development of an appropriate *monolithic* solver, modelling all multiphysical interactions simultaneously, the different time and length scales of each physical domain needs to be taken into account, resulting in a high computational cost. Conventional simulation techniques therefore limit themselves to a sequential approach, where the result of a first domain-specific solver is used in a second one. In this way only so-called *weak* one-way interactions are modelled, while *strong* two-way interactions are neglected.

A way to take the strong interactions into account, is a *partitioned* simulation approach. Such an approach starts from efficient domain-specific solvers, between which data is exhanged in both directions to model the multiphysical interactions. Partitioned approaches for the aeroacoustic-structural interaction were already developed in [7, 8], coupling an aeroacoustic solver and a structural solver. Their aeroacoustic solvers solve the compressible Navier-Stokes equations and simulate monolithically the strong two-way interaction between aerodynamics and acoustics. This results in a high computational cost, which limits the usage of these techniques to small computational domains. For flow-carrying structures like ventilation ducts and exhaust systems, the aeroacoustic simulation can be performed more efficiently using a *hybrid* approach, solving a linearized version of the compressible Navier-Stokes equations [9]. These linearized equations model the propagation and interaction of the aerodynamic and acoustic first-order fluctuations in the flow, while the mean flow parameters are considered known and steady. Such an approach is adopted in this work for modelling the *flow-acoustic* interaction. This term is preferred in this work over the term *aeroacoustic* to underline the difference with the solvers used in [7, 8].

As a first step towards the simulation of the flow-acoustic-structural interaction, this paper focuses on modelling the vibro-acoustic interaction by coupling an existing flow-acoustic and a structural solver. In section 2 the set-up of the partitioned approach is explained. Section 3 shows a verification case for the 2D vibro-acoustic interaction. Section 4 summarizes the main conclusions of the presented work.

2 Partitioned simulation approach

The partitioned simulation approach used in this work couples in the time domain a flow-acoustic solver for the linearized Euler equations and a structural solver for the Euler-Bernoulli beam equation. The kinematic and dynamic continuity at the interface between the different physical domains is ensured by a data exchange between the solvers at each time step. Subsection 2.1 gives more background about the flow-acoustic solver and subsection 2.2 about the structural solver. The communication scheme managing the data exchange during the time marching is explained in subsection 2.3. The spatial mapping allowing data transfer between non-matching meshes is clarified in subsection 2.4.

2.1 Flow-acoustic solver

The flow-acoustic interaction is modelled using an in-house solver for the Linearized Euler Equations (LEE) in the time domain [10, 11]. As the LEE make no assumptions regarding the nature of the pressure fluctuations, all linear interactions between aerodynamic and acoustic perturbations are accounted for. However, the mean flow profile will not be affected. In this work the mean flow is not yet taken into account and the LEE are therefore equivalent to the Acoustic Wave equation.

The time domain LEE can be written in matrix notation for a two-dimensional cartesian domain [11]:

$$\frac{\partial \boldsymbol{q}}{\partial t} + \frac{\partial \boldsymbol{F}_r}{\partial x_r} + \mathbb{C}\boldsymbol{q} = 0 \tag{1}$$

The Einstein's summation convention is used for r being one of the two cartesian coordinates ($x_1 = x, x_2 = y$). The unknown first-order fluctuations are indicated by $\boldsymbol{q}$, $\boldsymbol{F}_r = \mathbb{A}_r\boldsymbol{q}$ contains the flux Jacobians in the r-direction and the term $\mathbb{C}\boldsymbol{q}$ models the effects of a non-uniform mean flow:

$$\boldsymbol{q} = \begin{bmatrix} \rho \\ \rho_0 u_1 \\ \rho_0 u_2 \\ p \end{bmatrix}, \mathbb{A}_r = \begin{bmatrix} u_{0r} & \delta_{1r} & \delta_{2r} & 0 \\ 0 & u_{0r} & 0 & \delta_{1r} \\ 0 & 0 & u_{0r} & \delta_{2r} \\ 0 & c_0^2\delta_{1r} & c_0^2\delta_{2r} & u_{0r} \end{bmatrix}, \mathbb{C} = \begin{bmatrix} 0 & 0 & 0 & 0 \\ u_{0r}\frac{\partial u_{01}}{x_r} & \frac{\partial u_{01}}{x_1} & \frac{\partial u_{01}}{x_2} & 0 \\ u_{0r}\frac{\partial u_{02}}{x_r} & \frac{\partial u_{02}}{x_1} & \frac{\partial u_{02}}{x_2} & 0 \\ 0 & \frac{1-\gamma}{\rho_0}\frac{\partial p_0}{\partial x_1} & \frac{1-\gamma}{\rho_0}\frac{\partial p_0}{\partial x_2} & (\gamma-1)\frac{\partial u_{0r}}{\partial x_r} \end{bmatrix} \tag{2}$$

The perturbations ($\rho, \boldsymbol{u} = [u_1, u_2]^T, p$) and the mean flow parameters ($\rho_0, \boldsymbol{u}_0 = [u_{01}, u_{02}]^T, p_0$) indicate respectively the density, the velocity vector and the pressure. The speed of sound is calculated as $c_0^2 = \frac{\gamma p_0}{\rho_0}$ with γ the adiabatic index for air as an ideal gas. The symbol δ_{ij} indicates the Kronecker delta.

The nodal quadrature-free discontinuous Galerkin method is applied to spatially discretize the LEE over an unstructured straight-edge triangular grid. The in-depth discussion about the implementation can be found in [11]. Important to highlight is that within each element p^{th}-order Langrangian polynomials are used, interpolating between the nodal points which positions are chosen to optimize the interpolation characteristics [12]. The discontinuity of the nodal values $\hat{\boldsymbol{q}}$ over the edge $\partial\Omega_i$ between the element Ω^- and its neighbour element Ω^+ gives rise to a Riemann flux $\hat{\boldsymbol{F}}_R^{\partial\Omega_i}$. This numerical flux is implemented as the Lax-Friederich flux within the computational domain. At the boundary edge $\partial\Omega_b$ the numerical flux is adjusted to prescibe the boundary conditions:

$$\hat{\boldsymbol{F}}_R^{\partial\Omega_b} = \mathbb{A}_n^{\partial\Omega_b}\hat{\boldsymbol{q}}_{BC}^{\partial\Omega_b} \text{ with } \mathbb{A}_n^{\partial\Omega_b} = \sum_{r=1}^{2}\mathbb{A}_r^{\partial\Omega_b} n_r^{\partial\Omega_b} \tag{3}$$

The nodal values $\hat{\boldsymbol{q}}_{BC}^{\partial\Omega_b}$ are taken from the corresponding nodes in the boundary element Ω_b^-. For an anechoic inlet and outlet, the non-reflecting boundary condition is imposed by performing an eigendecomposition of the projected flux Jacobian $\mathbb{A}_n^{\partial\Omega_b}$ and maintaining only the outgoing characteristics. For a rigid wall, the slip condition ($\boldsymbol{u}\cdot\boldsymbol{n} = 0$), with $\boldsymbol{n}$ the outgoing normal, is prescribed by replacing in $\hat{\boldsymbol{q}}_{BC}^{\partial\Omega_b}$ the nodal velocity fluctuations by their tangential components: $\hat{\boldsymbol{u}} - (\hat{\boldsymbol{u}}\cdot\boldsymbol{n}^{\partial\Omega_b})\boldsymbol{n}^{\partial\Omega_b}$. For a flexible wall a normal nodal velocity $(\hat{\boldsymbol{v}}\cdot\boldsymbol{n}^{\partial\Omega_b})\boldsymbol{n}^{\partial\Omega_b}$ is imposed by the vibrating structure and summed to the tangential velocity fluctuations in $\hat{\boldsymbol{q}}_{BC}^{\partial\Omega_b}$. This flexible wall boundary condition assumes that no aerodynamic boundary layer is present. The effect of an infinitely thin boundary layer could be accounted for using the Ingard-Myers boundary condition [13], which expresses the continuity of wall normal displacement instead of normal velocity. However, this formulation is ill-posed in the time domain [14]. Well-posed time domain formulations are available in literature [15], but are not considered in this paper as the mean flow is not yet taken into account.

The temporal discretization is carried out with a low-memory storage explicit fourth order of accuracy Runge-Kutta scheme with eight stages, designated as RKC84 [16]. The stage coefficients are optimized for the discontinuous Galerkin spatial discretization. As it is an explicit method, the solution at the end of the time step is obtained solely from information available at the beginning of the time step. The time step is determined using a CFL condition based on the minimum height of the triangular elements [17].

2.2 Structural solver

To impose the normal velocities of the vibrating structure at the boundary of the flow-acoustic domain, the flow-acoustic solver is coupled to a linear elasto-dynamics solver in the time domain. As the flow-acoustic domain is 2D, the flexible wall can be modelled with the Euler-Bernoulli beam equation:

$$EI\frac{\partial^4 w(t,x_t)}{\partial x_t^4} + h\rho_s\frac{\partial^2 w(t,x_t)}{\partial t^2} = p_1(t,x_t) - p_2(t,x_t) \tag{4}$$

This equation describes the deformation w of a beam along the x_t-axis through time. The x_t-axis is tangential to the flexible wall boundary of the flow-acoustic domain and w indicates a displacement perpendicular to this axis. The Young's modulus of the linear elastic material is indicated by E, the density by ρ_s, the thickness by h and the second area moment by $I = \frac{h^3}{12}$. On each side of the x_t-axis a flow-acoustic domain can be situated, exerting a pressure force $p_1 - p_2$ on the beam.

Spatial discretization is done with the isoparametric finite element method, as described in [18]. The beam is divided into beam elements of equal length with each 2 nodes. The boundary conditions for a clamped beam are enforced by setting the nodal value for the displacement w and the rotation $\theta = \frac{dw}{dx_t}$ at the beam's ends on zero.

The time integration is performed following the Newmark-Beta's algorithm, described in [18]. By choosing the algorithm's coefficients as $\beta = 1/4$ and $\alpha = 1/2$, this implicit algorithm is unconditionallly stable and known as the *method of constant acceleration*. The time step size determines the accuracy in terms of numerical dissipation and dispersion. Due to its implicit character, the flow-acoustic pressures at the end of the time step need to be known at the start of the time step.

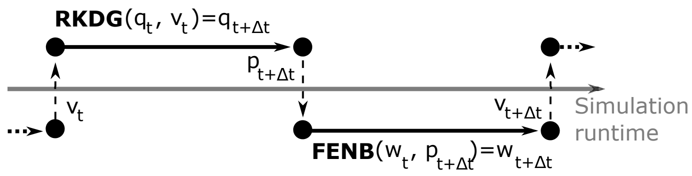

Figure 1: Illustration of the communication during runtime for one common time step Δt following the Conventional Serial Staggered scheme (CSS). RKDG stands for Runge-Kutta Discontinuous Galerkin and FENB stands for Finite Elements Newmark-Beta.

2.3 Time domain coupling

The flow-acoustic and structural solver are run in a co-simulation. This means that a common time step needs to be defined to keep both solvers synchronized. At the end of such a common time step, data is exchanged between both solvers to ensure kinematic and dynamic continuity over the interface. The pressure fluctuations acting on the flexible wall boundary of the flow-acoustic mesh are transferred to the structural model and the normal velocity of the flexible wall is communicated in the other direction. It is assumed that the structural deformations are small and the flow-acoustic mesh does not change over time. The time steps of both solvers can be chosen according to the solver's own stability and accuracy rules. The common time step can then be set equal to the largest time step, such that the solver with the smaller time step subcycles until it reaches the end of the common time step. During these subcycles predictions for the evolution of the other solver's data can be made to increase the accuracy [8].

The communication between the flow-acoustic solver and the structural solver is realized with a Conventional Serial Staggered scheme (CSS), as shown in Figure 1. The explicit Runge-Kutta scheme of the flow-acoustic solver requires the wall velocity v_t at the beginning of the common time step. On the other hand, the implicit Newmark-Beta scheme of the structural solver requires the pressure load $p_{t+\Delta t}$ at the beginning of the common time step. The flow-acoustic solver is therefore run first until the end of the common time step. The computed wall pressures are then communicated to the structural solver, which then completes its time marching until the end of the common time step. At that point, the wall normal velocity is communicated back to the flow-acoustic solver and the process is repeated. As decribed in [19], for a compressible fluid the CSS scheme is stable and should obtain an order of accuracy comparable to a monolithic method in the limit of a vanishing common time step size. Algorithms for repeating each common time step until convergence can be used if the benefits in terms of accuracy outweighs the added computational cost. The CSS scheme is managed through the routines of the open-source library preCICE [20], licensed under LGPL3. This results in only high-level adaptations in the source code of the solvers.

2.4 Spatial mapping

The spatial discretization of the flow-acoustic and structural domain are independent from each other. This means that at the interface the nodal positions from the flow-acoustic mesh (total amount n_a) do not match the ones of the structural mesh (total amount n_s). Hence, the nodal values need to be mapped each common time step. The mapping from flow-acoustic mesh to the structural mesh is represented by the $(n_s \times n_a)$ matrix $\mathbb{H}_{sa}$ and in the other direction by the $(n_a \times n_s)$ matrix $\mathbb{H}_{as}$:

$$\hat{\boldsymbol{p}}_1 - \hat{\boldsymbol{p}}_2 \equiv \hat{\boldsymbol{P}}_s = \mathbb{H}_{sa}\hat{\boldsymbol{P}}_a \tag{5}$$

$$\hat{\boldsymbol{v}} \equiv \hat{\boldsymbol{V}}_a = \mathbb{H}_{as}\hat{\boldsymbol{V}}_s \tag{6}$$

To define these mapping matrices different approaches are known in literature [21, 22]. These approaches are determined by a mapping constraint and a mapping method. The mapping constraint can be *consistent* or *conservative*. A consistent mapping exactly transfers a constant function between two non-matching meshes and is used for parameters like velocity. The corresponding constraint to the mapping matrix is that each row sum equals one. Conservative mappings preserve the total sum of a parameter over the interface and are

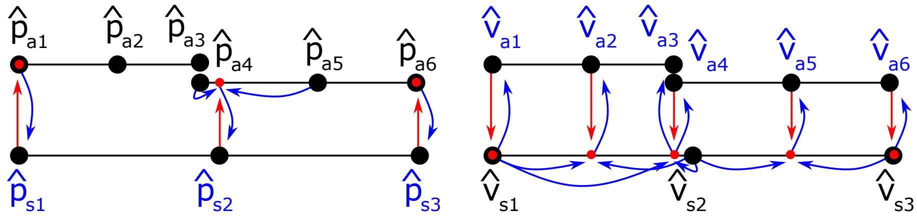

Figure 2: Illustration of the consistent Nearest Projection mapping, assuming that the flexible wall boundary of the flow-acoustic mesh (top line) exists of 2 elements and the structural mesh (bottom line) has also 2 elements. For simplifying the figure, the flow-acoustic and structural element sizes are taken almost equal and the order p of the flow-acoustic mesh is 2. The red arrows indicate the orthogonal projection of the target mesh on the source mesh and the blue arrows illustrate the linear interpolation and the copying of the value onto the target mesh.

used for parameters like forces. The constraint to the mapping matrix is then that each column sum equals one. To map pressures, which are distributed forces, the consistent constraint is used in this paper.

Conform the chosen constraint, the mapping method further defines the mapping matrix. Several methods exist in literature and a classification based on [21, 22] is given. A first class are the projection-based methods, which includes the simplest kind of mapping, namely Nearest Neighbour mapping. As the name indicates, each node gets the value from its nearest neighbour in the other mesh. This method only has first order accuracy. A better choice is then the Nearest Projection mapping, which works as shown in Figure 2. The nodes of the target mesh are orthogonally projected on the source mesh, where the projected image gets its value by linear interpolation between the neighbouring source mesh nodal values. This value is then copied back to the target mesh. When the projected image coincides with a source mesh node, no interpolation is necessary. The Nearest Projection mapping is second order accurate. To increase the order of accuracy, the Nearest Projection mapping can be extended by using the solver's higher-order shape functions for the interpolation. A further extension is the Weighted Residual mapping, which determines the mapping matrix out of a weak formulation of the mapping residual with as weighing functions the solver's shape functions.

A second class of mapping methods is the Radial Basis Function mapping. This approach constructs a global interpolant over the source mesh out of radially symmetric basis functions at its nodes. The interpolant can then be directly evaluated at the target mesh nodes. The order of accuracy depends on the chosen radial basis functions. These mapping methods are computationally more efficient than the projection-based mapping methods as they do not need a projection and search algorithm.

The spatial mapping is managed through the routines of the open-source library preCICE [20]. As preCICE regards each domain-specific solver as a black-box, it does not know the solver's shape functions. Therefore it only provides consistent and conservative implementations of the Nearest Neighbour, Nearest Projection and Radial Basis Function mapping. The mapping matrices only need to be computed once, as the meshes do not change assuming small vibrational amplitudes.

3 2D vibro-acoustic verification case

The verification case describes the propagation of plane acoustic waves through a 2D duct with a flexible side wall backed by a cavity and is simulated with the developed partitioned model and with a monolithic reference model. A two-port characterization of the flexible wall duct segment is used to facilitate the comparison of the results. Subsection 3.1 presents the geometry and some analytical considerations. The model settings for the partitioned approach are given in subsection 3.2 and in subsection 3.3 for the reference model. The two-port characterization is explained in subsection 3.4 and subsection 3.5 discusses the results.

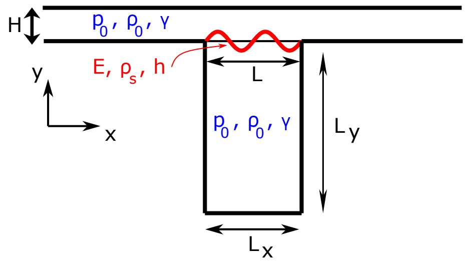

Figure 3: Geometry of the 2D vibro-acoustic verification case.

3.1 Geometry and analytical cosiderations

The geometry of the verification case is shown in Figure 3. The duct has a length of 3 m and a height H of 0.04 m. A duct segment with a length L of 0.2 m has a flexible wall backed by a cavity. The remaining walls of the cavity and the duct are modelled as rigid. The ambient pressure p_0 and density ρ_0 of the fluid are respectively 101.325 kPa and 1.225 kg/m^3, which makes the speed of sound c_0 equal to 340.3 m/s. Acoustic plane wave propagation can be assumed in the duct below the first cut-on frequency $f_{cut-on,1}$ [23]:

$$f_{cut-on,1} = \frac{c_0}{2H} = 4253.75\,\text{Hz} \tag{7}$$

Only the plane acoustic wave region is considered in this paper. The backing cavity has a width L_x of 0.2 m and a height L_y of 0.45 m. Under the assumption of rigid walls the first two cavity modes are determined analytically at 378.1 Hz ($m = 1, n = 0$) and at 756.2 Hz ($m = 2, n = 0$) [23]:

$$f_{cavity,(m,n)} = \frac{c_0}{2\pi}\sqrt{\left(\frac{n\pi}{L_x}\right)^2 + \left(\frac{m\pi}{L_y}\right)^2} \tag{8}$$

The beam is made out of steel with a Young's modulus E equal to 233.1 GPa and a density ρ_s of 7766.9 kg/m^3. It has a length L of 0.2 m and a thickness h equal to 0.5 mm. The beam is clamped on both sides and the first four beam modes following the analytical in-vacuo solution lie at 70.4 Hz, 194 Hz, 380.4 Hz and 628.8 Hz [24]:

$$f_{beam,s} = \frac{k_s^2}{2\pi}\sqrt{\frac{EI}{h\rho}} \text{ with } k_s \text{ the } s^{th} \text{ solution of } cos(k_sL) = sech(k_sL) \tag{9}$$

At very high frequencies the structural wavelengths of the beam become sufficiently short to describe them as a propagating flexural wave. Important for the vibro-acoustic interaction is in that case the coincidence frequency f_c. This is the frequency at which the structural wavelength λ_b equals the acoustic wavelength λ. The beam becomes then transparent for the acoustic waves. The coincidence frequency lies for this beam at 23.309 kHz [25], which is well above the frequency range of interest:

$$f_c = \frac{c_0^2}{2\pi}\sqrt{\frac{\rho h}{EI}} \tag{10}$$

3.2 Partitioned time domain model

As described in section 2, the partitioned approach divides the computational domain into a flow-acoustic and a structural domain with each a domain-specific solver. A schematic of this decomposition for the verification case can be seen in Figure 4. The solver coupling is realized through the flexible wall boundary condition of Equation 3 in the flow-acoustic model and the pressure loads in Equation 4 in the structural model. In the flow-acoustic model, the anechoic inlet and outlet of the duct are modelled with the non-reflecting characteristic boundary condition and the slip boundary condition is imposed at the rigid walls of

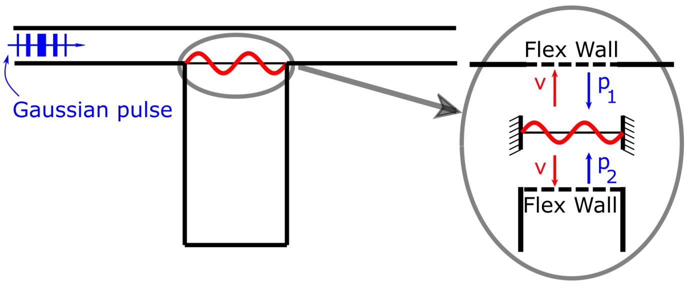

Figure 4: Schematic overview of the 2D vibro-acoustic verification case and the partitioned modelling approach. A plane Gaussian acoustic pulse propagates through the duct and initiates the vibro-acoustic interaction between the acoustic field in the duct and cavity and the structural vibrations of the beam.

the duct and the cavity. In the structural model, the beam's ends are represented by a clamped boundary condition.

As indicated in subsections 2.3 en 2.4, the element size and time step size of the two solvers do not need to match, which is an important instrument to lower computational cost and a key argument for the development of a partitioned solver. As only the plane acoustic wave region is considered in this work, the frequencies of interest are well below the coincidence frequency of the beam and the excited structural waves cannot be seen as propagating flexural waves, but only as standing waves. Therefore the structural solver can have a larger element size and a larger time step size than the flow-acoustic solver. The choice has however been made to take the element size and the time step size of both solvers equal in this paper, such that the partitioned method and the monolithic reference method can be properly compared.

For the element size a characteristic length of 0.01 m has been chosen, resulting in 5404 flow-acoustic elements and 20 structural elements. For both solvers independently these grids are overly fine. The flow-acoustic mesh is made out of straight-edge triangles and the nodes at the triangle edge vertices on the flexible wall boundary match the nodal positions in the structural mesh. So the mapping of the pressure values from the flow-acoustic mesh to the structural mesh is exact. For the mapping of the velocity values from the structural mesh to the flow-acoustic mesh, the values at the flow-acoustic nodes in between the triangle edge vertices due to the higher-order shape functions still need to be determined. In this work, the order p is chosen as 5, giving 4 extra nodes on the triangle edge, and the consistent Nearest Projection Mapping is used. The time step size of both solvers, thus also the common time step, is set as 1.47 µs based on the minimum height CFL rule of the flow-acoustic solver [17]. No solver needs to subcycle and also no iterative algorithm to reach convergence each common time step is used.

One of the advantages of a time domain simulation is the capability of assessing the system's behavior over a broad frequency range by exciting the system with a pulse and monitoring its broadband response. In this verification case a Gaussian acoustic pulse excitation is imposed at the duct inlet. The pulse propagates through the duct as a plane wave and initiates a vibro-acoustic interaction with the beam and the cavity. The system's response is monitored at several positions located on the centerline of the duct.

3.3 Monolithic reference model

A reference solution for the verification of the 2D vibro-acoustic case is obtained using the frequency domain finite element model of COMSOL Multiphysics 5.4.

In the acoustic domain the Helmholtz equation is solved over an unstructured straight-edge triangular grid, existing of 5054 elements. A Perfectly Matched Layer is put at the inlet and outlet of the duct and meshed with a structured grid of 40 rectangles on each side. The slip boundary condition is defined at the rigid walls. A time-harmonic pressure source at the inlet excites plane acoustic waves, propagating through the duct. The dynamics of the beam are modelled by the equations of motion in the frequency domain for a linear elastic material with the fixed boundary condition at the outer ends. The plane stress assumption is used such

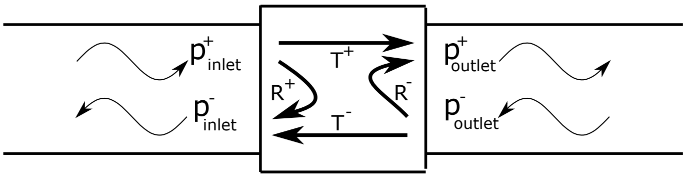

Figure 5: Schematic overview of the two-port element and the scattering matrix coefficients $T^{\pm}$ and $R^{\pm}$, representing the amplitude and phase change that incoming plane waves undergo in the black-box.

that the solution is equivalent to the one of the Euler-Bernoulli beam equation. The structural domain is a structured mesh with 5 rows of 80 rectangular elements. The Acoustics-Structure boundary condition is set at the interfaces between both physical domains and enforces the continuity of pressure and normal velocity.

The acoustic and structural models are discretized with the finite element method, creating a single system matrix that is solved in the chosen frequency range to determine the time-harmonic response of the system. This is thus a monolithic vibro-acoustic approach. The acoustic and structural meshes match at their interace such that no data mapping is necessary. To ensure conformity at this interface, the same Quadratic Langrangian shape functions are used in both domains.

3.4 Duct acoustic characterization

A two-port characterization of the duct segment with the flexible wall and cavity is used to analyze the simulation results and to facilitate the comparison between the monolithic frequency domain model and the partitioned time domain approach. This method regards the duct segment with the flexible wall and cavity as a black-box element and characterizes it by a linear input-output relation in the frequency domain, which is independent of the boundary conditions and sources at the inlet and outlet of the duct. Below the first cut-on frequency of the duct, these inputs and outputs are described in terms of the complex amplitudes p^+ and p^- of the right-running and left-running plane acoustic waves.

The vibro-acoustic interaction within the duct segment is then described by the scattering matrix:

$$\begin{bmatrix} p^+_{outlet}(f) \\ p^-_{inlet}(f) \end{bmatrix} = \begin{bmatrix} T^+(f) & R^-(f) \\ R^+(f) & T^-(f) \end{bmatrix} \begin{bmatrix} p^+_{inlet}(f) \\ p^-_{outlet}(f) \end{bmatrix} \tag{11}$$

The scattering of the plane acoustic waves is expressed in terms of transmission $T^{\pm}$ and reflection coefficients $R^{\pm}$ as can be seen in Figure 5. In the frequency domain simulation in COMSOL, it is possible to request the incident and scattered pressure values directly. Given the anechoic boundary conditions, the transmission and reflection coefficients are easily determined by dividing the scattered pressure values at the outlet, respectively the inlet of the duct by the incident plane acoustic wave.

In the partitioned time domain simulation, the response of the system to the incident Gaussian plane pulse is sampled at several positions along the duct centerline. The simulation is stopped after approximately 0.3 s. The saved time signals are then transformed to the frequency domain with a FFT. Due to the excitation of the beam and cavity resonances without any damping mechanism except numerical dissipation, a half-Hanning window is needed to let the pressure values at the end of the simulation time converge to zero. The frequency content of the time signals at the sampling points is used to decompose the acoustic field into the left- and right-running plane waves and to determine the scattering matrix coefficients by solving linear systems of equations [26].

3.5 Discussion of the results

The transmission and reflection coefficients obtained with the partitioned and the monolithic simulation are shown in Figure 6 for frequencies up to 850 Hz. At a first glance, it is clear that the different beam and cavity modes are the main drivers of the vibro-acoustic interaction. However some important differences are visible

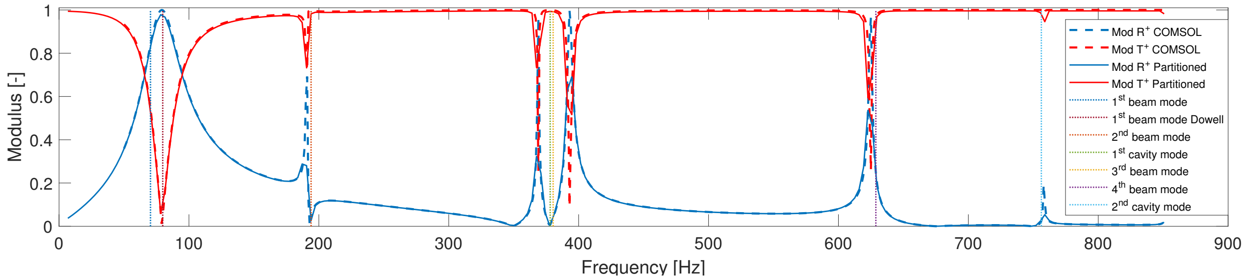

Figure 6: Modulus of the complex transmission and reflection coefficients in the frequency domain for the verification case, obtained from the developed partitioned time domain approach and compared to the solution from a commercial monolithic frequency domain Finite Element solver (COMSOL Multiphysics 5.4).

from the analytical resonance frequencies given in subsection 3.1. These differences can be summarized into two strong vibro-acoustic coupling effects.

The first one is the change in resonance frequency of the beam modes due to the presence of the cavity. When the resonance frequency of the cavity mode $\phi_{(m,n)}$ lies higher than the one of the beam mode ψ_s, the cavity adds an equivalent mass to the beam, lowering the beam resonance frequency. When the resonance frequency of cavity mode $\phi_{(m,n)}$ lies lower than the one of the beam mode ψ_s, the cavity increases the structural stiffness and therefore the beam resonance frequency. The cavity mode $\phi_{(0,0)}$ thus always adds stiffness to the beam mode ψ_s and this effect can be determined analytically following Dowell's work [27]:

$$f_{beam,s,shifted} = \frac{1}{2\pi}\sqrt{(2\pi f_{beam,s})^2 + \frac{\rho_0 c_0^2 L^2 Q_{0s}^2}{M_s L_x L_y}} \tag{12}$$

with:

$$Q_{0s} = \frac{1}{L}\int_L \phi_{(0,0)}\psi_s dx$$
$$M_s = \int_L \rho h \psi_s \psi_s dx$$
$$\phi_{(0,0)} = 1, \quad \psi_s(x) = cosh(k_s x) - cos(k_s x) - \frac{cosh(k_s L) - cos(k_s L)}{sinh(k_s L) - sin(k_s L)}(sinh(k_s x) - sin(k_s x))$$

For the first beam mode, this results in a shift of the resonance frequency from 70.4 Hz to 79.8 Hz, which confirms the shift visible in Figure 6. For the shifts in frequency of the second and fourth beam mode, the influence of the first and second cavity mode should also be taken into account, making the analytical formulation by Dowell incomplete.

The second effect is the coupling of a cavity mode with a beam mode with coinciding resonance frequencies. This happens here for the third beam mode and the first cavity resonance around 380 Hz. The coinciding resonance frequencies then lead to the tuned vibration absorber effect: at the original resonance frequency both resonances cancel each other out and two new resonance peaks arise, here at 369 Hz and 393 Hz.

The results show that the partitioned approach manages to properly capture these strong vibro-acoustic coupling effects. The peaks in the graphs for the partitioned approach are however less sharp than in the ones for the monolithic method. This is due to the energy that stays behind in the resonating modes when the simulation ends and the damping introduced by the half-Hanning window. Running the simulation longer will result in better convergence of the time signals to zero and sharper peaks for this verification case. In more realistic cases, this issue will be solved by the addition of damping in the structural model.

4 Conclusions

This paper describes the coupling of a flow-acoustic solver for the linearized Euler equations and a structural solver for the Euler-Bernoulli beam equation in the time domain with the goal of developing a simulation tool for the flow-acoustic-structural interaction in flow-confining structures. The main advantage of such a partitioned approach is that it allows each solver to have its own spatial and temporal discretization schemes, such that the different time and length scales in each physical domain can be dealt with in an efficient way. The exchange of data between both solvers, requiring mapping and synchronization algorithms, is realized using the algorithms available in the open-source library preCICE [20], licensed under LGPL3.

The focus lies in this work on the vibro-acoustic verification of the partitioned approach in 2D. No mean flow is taken into account. The data exchanged between both solvers needs to ensure the kinematic continuity of normal velocity and the dynamic continuity of pressure over their interface. This is obtained by transferring the nodal pressure values at the flexible wall boundary of the flow-acoustic mesh to the nodes of the structural mesh. The normal velocity of the flexible wall is communicated in the other direction. This data exchange follows the Conventional Serial Staggered communication scheme (CSS). The mapping between both meshes happens following the consistent Nearest Projection method.

The partitioned approach is verified by comparing the results of a 2D case with the results from a monolithic commercial solver. This case simulates the propagation of plane acoustic waves through a duct segment with one flexible wall backed by a cavity. The transmission and reflection coefficients, obtained by applying the two-port characterization method to the simulation results, show that the partitioned approach properly captures the strong vibro-acoustic interactions.

Acknowledgements

The research of Jurgen Kersschot (fellowship no. 1SA6719N) is funded by a grant from the Research Foundation – Flanders (FWO). The Research Fund KU Leuven is gratefully acknowledged for its support.

References

[1] M. K. Bull, “Wall-pressure fluctuations beneath turbulent boundary layers: some reflections on forty years of research,” *Journal of Sound and vibration*, vol. 190, no. 3, pp. 299–315, 1996.

[2] A. Cummings, “Sound transmission through duct walls,” *Journal of Sound and Vibration*, vol. 239, no. 4, pp. 731–765, 2001.

[3] N. Jade and B. Venkatesham, “Experimental study of breakout noise characteristics of flexible rectangular duct,” *Mechanical Systems and Signal Processing*, vol. 108, pp. 156–172, 2018.

[4] L. Huang, “A theoretical study of duct noise control by flexible panels,” *the Journal of the Acoustical Society of America*, vol. 106, no. 4, pp. 1801–1809, 1999.

[5] M. M. Sucheendran, D. J. Bodony, and P. H. Geubelle, “Coupled structural-acoustic response of a duct-mounted elastic plate with grazing flow,” *AIAA journal*, vol. 52, no. 1, pp. 178–194, 2014.

[6] A. David, F. Hugues, N. Dauchez, and E. Perrey-Debain, “Vibrational response of a rectangular duct of finite length excited by a turbulent internal flow,” *Journal of Sound and Vibration*, vol. 422, pp. 146–160, 2018.

[7] H. K. H. Fan, R. C. K. Leung, and G. C. Y. Lam, “Numerical analysis of aeroacoustic-structural interaction of a flexible panel in uniform duct flow,” *The Journal of the Acoustical Society of America*, vol. 137, no. 6, pp. 3115–3126, 2015.

[8] J. Richard and F. Nicoud, “Effect of the fluid structure interaction on the aeroacoustic instabilities of solid rocket motors,” in *17th AIAA/CEAS Aeroacoustics Conference (32nd AIAA Aeroacoustics Conference)*, 2011, p. 2816.

[9] W. De Roeck, “Hybrid methodologies for the computational aeroacoustics analysis of confined subsonic flows,” Ph.D. dissertation, KU Leuven, 2007.

[10] Y. Reymen, “3D high-order discontinuous Galerkin methods for time-domain simulation of flow noise propagation,” Ph.D. dissertation, KU Leuven, 2008.

[11] T. Toulorge, “Efficient Runge-Kutta discontinuous Galerkin methods applied to aeroacoustics,” Ph.D. dissertation, KU Leuven, 2012.

[12] J. S. Hesthaven, “From electrostatics to almost optimal nodal sets for polynomial interpolation in a simplex,” *SIAM Journal on Numerical Analysis*, vol. 35, no. 2, pp. 655–676, 1998.

[13] M. K. Myers, “On the acoustic boundary condition in the presence of flow,” *Journal of Sound and Vibration*, vol. 71, no. 3, pp. 429–434, 1980.

[14] E. J. Brambley, “Fundamental problems with the model of uniform flow over acoustic linings,” *Journal of Sound and Vibration*, vol. 322, no. 4-5, pp. 1026–1037, 2009.

[15] E. J. Brambley, “Well-posed boundary condition for acoustic liners in straight ducts with flow,” *AIAA journal*, vol. 49, no. 6, pp. 1272–1282, 2011.

[16] T. Toulorge and W. Desmet, “Optimal Runge–Kutta schemes for discontinuous Galerkin space discretizations applied to wave propagation problems,” *Journal of Computational Physics*, vol. 231, no. 4, pp. 2067–2091, 2012.

[17] T. Toulorge and W. Desmet, “CFL conditions for Runge–Kutta discontinuous Galerkin methods on triangular grids,” *Journal of Computational Physics*, vol. 230, no. 12, pp. 4657–4678, 2011.

[18] M. A. Neto, A. Amaro, L. Roseiro, J. Cirne, and R. Leal, *Engineering computation of structures: the finite element method*. Springer, 2015.

[19] E. H. van Brummelen, “Added mass effects of compressible and incompressible flows in fluid-structure interaction,” *Journal of Applied mechanics*, vol. 76, no. 2, 2009.

[20] H.-J. Bungartz, F. Lindner, B. Gatzhammer, M. Mehl, K. Scheufele, A. Shukaev, and B. Uekermann, “preCICE–a fully parallel library for multi-physics surface coupling,” *Computers & Fluids*, vol. 141, pp. 250–258, 2016.

[21] A. de Boer, A. H. van Zuijlen, and H. Bijl, “Comparison of conservative and consistent approaches for the coupling of non-matching meshes,” *Computer Methods in Applied Mechanics and Engineering*, vol. 197, no. 49-50, pp. 4284–4297, 2008.

[22] B. Gatzhammer, “Efficient and flexible partitioned simulation of fluid-structure interactions,” Ph.D. dissertation, Technische Universität München, 2014.

[23] A. D. Pierce, *Acoustics: An introduction to its physical principles and applications*. Acoustical Society of America, 1989.

[24] S. S. Rao, *Vibration of continuous systems*. Wiley Online Library, 2007.

[25] M. P. Norton and D. G. Karczub, *Fundamentals of noise and vibration analysis for engineers*. Cambridge university press, 2003.

[26] H. Denayer, “Flow-acoustic characterization of duct components using multi-port techniques,” Ph.D. dissertation, KU Leuven, 2017.

[27] E. H. Dowell, G. F. Gorman, and D. A. Smith, “Acoustoelasticity: General theory, acoustic natural modes and forced response to sinusoidal excitation, including comparisons with experiment,” *Journal of Sound and vibration*, vol. 52, no. 4, pp. 519–542, 1977.